HHS Public Access

Author manuscript

Nat Biomed Eng. Author manuscript; available in PMC 2019 August 18.

Published in final edited form as:

Nat Biomed Eng. 2019 April ; 3(4): 281–291. doi:10.1038/s41551-019-0358-7.

Non-invasive early detection of acute transplant rejection via nanosensors of granzyme-B activity

Quoc D. Mac[#1], **Dave V. Mathews**[#6], **Justin A. Kahla**[1], **Claire M. Stoffers**[1], **Olivia M. Delmas**[1], **Brandon Alexander Holt**[1], **Andrew B. Adams**[6,7,*], and **Gabriel A. Kwong**[1,2,3,4,5,*]

[1]Wallace H. Coulter Department of Biomedical Engineering, Georgia Tech College of Engineering and Emory School of Medicine, Atlanta, GA 30332, USA.

[2]Parker H. Petit Institute of Bioengineering and Bioscience, Atlanta, GA 30332, USA.

[3]Institute for Electronics and Nanotechnology, Georgia Tech, Atlanta, GA 30332.

[4]Integrated Cancer Research Center, Georgia Tech, Atlanta, GA 30332.

[5]The Georgia Immunoengineering Consortium, Emory University and Georgia Tech, Atlanta, GA 30332.

[6]Emory Transplant Center, Emory University, Atlanta, GA 30322.

[7]Department of Surgery, Emory University School of Medicine, Atlanta, GA 30322.

[#] These authors contributed equally to this work.

Abstract

The early detection of the onset of transplant rejection is critical for the long-term survival of patients. The diagnostic gold-standard for detecting transplant rejection involves a core biopsy, which is invasive, has limited predictive power, and carries a morbidity risk. Here, we show that nanoparticles conjugated with a peptide substrate specific for the serine protease granzyme B, which is produced by recipient T cells during the onset of acute cellular rejection, can serve as a non-invasive biomarker of early rejection. Upon systemic administration in mouse models of skin-graft rejection, these nanosensors preferentially accumulate in allograft tissue, where they are cleaved by granzyme B, releasing a fluorescent reporter that filters into the recipient's urine. Urinalysis then discriminates the onset of rejection with high sensitivity and specificity before

[*]To whom correspondence should be addressed: gkwong@gatech.edu (G.A.K.), andrew.b.adams@emory.edu (A.B.A.).

Author contributions

Q.D.M., D.V.M., A.B.A, and G.A.K conceived of the idea, designed experiments, and interpreted results. Q.D.M., D.V.M., J.A.K., C.M.S., O.M.D., B.A.H. carried out the experiments. Q.D.M., D.V.M., B.A.H., A.B.A., and G.A.K. wrote the manuscript.

Competing interests

Q.D.M., D.V.M., A.B.A. and G.A.K are listed as inventors on a patent application pertaining to the results of the paper. G.A.K. is co-founder of and serves as consultant to Glympse Bio, which is developing products related to the research described in this paper. This study could affect his personal financial status. The terms of this arrangement have been reviewed and approved by Georgia Tech in accordance with its conflict of interest policies.

Data availability

All data supporting the findings of this study are available within the manuscript and its Supplementary Information. Raw data are available from the corresponding authors.

features of rejection are apparent in grafted tissues. Moreover, in mice treated with subtherapeutic levels of immunosuppressive drugs, the reporter signals in urine can be detected before graft failure. This method may enable routine monitoring of allograft status without the need for biopsies.

Organ transplantation remains the single most effective treatment for end-stage organ failure, and early detection of transplant rejection is critical for managing immunosuppression and the long-term survival of recipients [1,2]. During acute cellular rejection (ACR), graft damage is mediated by recipient cytotoxic CD8 T cells that are activated by alloantigens displayed by antigen presenting cells (APC) and target allogeneic cells for killing [3,4]. Although ACR episodes may appear at any time during the life of the graft even years after immunological quiescence [5], ACR can be effectively treated with anti-rejection drugs that target T cells (e.g., cyclosporine, thymoglobulin, or anti-CD3 antibodies). Therefore the ability to measure the level of anti-graft T cell responses at an early stage of ACR plays an indispensable role in managing long-term graft health and function [6]. Currently, the gold standard for diagnosing ACR is the core tissue biopsy, but this procedure is invasive, subject to sampling error (tissue specimen typically represents ~1/10,000th the volume of the organ), and associated with potential patient morbidity [7,8]. Noninvasive approaches include measuring biomarkers that indicate organ dysfunction, such as blood urea nitrogen (BUN) and serum creatinine for kidney allografts [9,10], or biomarkers associated with allograft cell death, such as cell-free donor-derived DNA from the blood of heart transplant patients [11]. These biomarkers indicate graft health at a stage of rejection when organ dysfunction or damage is clinically apparent.

The mechanism by which activated cytotoxic T cells engage and kill target cells is well studied and involves the release of cytolytic granules containing perforin, which forms pores in target cell membranes, and granzymes (Gzm), which are serine proteases, to trigger apoptosis by cleavage of caspases or activation of mitochondria and DNA damage pathways [4,12]. Early onset ACR or subclinical ACR, defined according to Banff stage T cell mediated rejection (TCMR) IA and IB, have been directly shown to correlate to increased Granzyme B (GzmB) expression [13–15]. In renal allografts, the level of GzmB+ lymphocytes are significantly higher in stages IA and IB compared to control biopsies [13,14], and predict rapid progression to severe ACR (TMCR grade II or higher) [13]. Clinical studies focused on quantifying RNA transcripts showed that elevated GzmB levels in blood or urine are correlated to early ACR (grade IB or lower) and precede clinical diagnosis of ACR in renal and islet transplant patients [16–19]. Importantly, the activity of GzmB is also regulated by tissues locally; increased expression of the endogenous GzmB inhibitor serpin protease inhibitor 9 (PI-9) [20] was reported to be a potential mechanism for stable renal function in patients with subclinical ACR [14] by inhibiting the ability of GzmB to trigger apoptosis in target cells. These clinical studies provide direct support for targeting GzmB as an early indicator of ACR, and motivate the need to develop new methods to measure the activity of GzmB within the context of the local tissue microenvironment.

A promising approach to noninvasively measure *in vivo* protease activity is the design and administration of engineered agents to interrogate diseased tissue. These include activity-

based imaging probes that emit fluorescent signals upon cleavage [21], or selectively bind to the active state of proteases [22]. Recently, this approach was employed for *in vivo* imaging of GzmB activity during experimental myocarditis and monitoring the treatment efficacy of cancer immunotherapy with positron emission tomography (PET) probes that irreversibly bind to GzmB [23,24]. Activity-based approaches using fluorescent reporters are limited to superficial sites by tissue scattering, but can be used in deeper tissues with invasive procedures, such as during tumor resection [25,26]. Here we engineer GzmB nanosensors that accumulate in allograft tissue to sense anti-graft T cell activity by producing a signal that is shed into recipient urine for noninvasive detection (Figure 1). Our technology builds on our work on synthetic biomarkers [27–31], which leverage the catalytic activity of proteases to amplify detection signals, as well as the enrichment of detection signals into urine to allow ultrasensitive detection of early stage disease. In preclinical skin graft models of rejection, our GzmB activity nanosensors allow noninvasive discrimination of early ACR and indicate graft failure in recipients under subtherapeutic immunosuppression.

Results

Engineering activity nanosensors against Granzyme B

Our activity nanosensors are formulated by conjugating GzmB peptide substrates to the surface of a nanoparticle scaffold (Figure 2A). A nanoparticle carrier extends the circulation half-life of GzmB peptide substrates (Supplemental Figure S1) [32], which would otherwise be rapidly filtered into urine, and increases peptide accumulation in tissues by passive diffusion from the circulating vasculature. Protease cleavage of the nanosensor by GzmB triggers a pharmacokinetic switch by releasing peptide fragments locally, which are then remotely cleared into urine for noninvasive detection. Here we used iron oxide nanoparticles (IONP) because it is well-tolerated and FDA-approved for clinical use as anemia therapies, contrast agents, and thermal ablation [33,34]. To increase biocompatibility and circulation half-life, we decorated IONPs synthesized in house [35] with polyethylene glycol (PEG) to reduce nanoparticle uptake by the reticuloendothelial system (RES) [36]. With moderate PEGylation (20:1 PEG to IONP ratio), the average hydrodynamic diameter of our IONPs was ~47 nm while the circulation half-life was increased to ~3 hour *in vivo* (Supplemental Figure S2). These values are consistent with previously reported values for clinically approved IONPs [34].

To identify peptide substrates that are sensitive to cleavage by recombinant GzmB, we pooled 13 candidate substrates from published literature [37–40] (Supplemental Figure S3). These substrates were 6–12 amino acids in length and characterized by a consensus cleavage motif with isoleucine at position P4 and aspartic acid at P1 immediately N-terminal of the cleavage site. From our library, the substrate sequence AIEFD|SG resulted in the highest initial cleavage velocity by recombinant GzmB (Supplemental Figure S3). To determine cleavage efficiency of peptide substrates conjugated to a nanoparticle, we conducted Michaelis-Menten kinetic analysis and calculated a k_{cat}/K_M value of 1.09×10^4 $M^{-1}s^{-1}$. This value was similar in magnitude to reported values of GzmB cleavage of free substrates (Figure 2B) [37,40] and showed that co-presentation of substrates and PEG molecules (Supplemental Figure S4) on the surface of IONPs did not sterically hinder GzmB cleavage.

To assess substrate specificity for GzmB, we exposed our probes to coagulation and complement proteases because they are ubiquitous and found at high concentrations in circulating blood. Using saline samples spiked with recombinant proteases (Figure 2C), plasma samples spiked with Ca^{2+} to trigger coagulation (Figure 2D; Supplemental Figure S5), or heat aggregated gamma globulin (HAGG) to trigger complement (Figure 2E, F), we did not observe detectable increases in fluorescence that would indicate cross-cutting of our probes. By contrast, our probes were markedly activated in all samples that contained recombinant GzmB. To further test the biocompatibility of our nanosensors, we assessed the level of membrane attack complex (MAC) in serum samples to quantify potential complement activation from a foreign surface. We found significant increase in MAC levels in samples incubated with HAGG, but by contrast, no elevation in MAC formation in the presence of our probes (***P, n = 3, Figure 2F). Taken together, our activity nanosensors are sensitive to GzmB cleavage, are not cross-cut by coagulation and complement cascades, and do not promote complement activity.

GzmB activity nanosensors detect alloreactive T cell killing

During target cell killing, an immune synapse is formed between cytotoxic T lymphocytes (CTLs) and target cells, and cytotoxic granules are directionally released into the synaptic cleft. This mechanism is thought to increase the local concentration of effector molecules to enhance target cell entry and killing, as well as to decrease off-target cytotoxicity by limiting exposure of bystander cells to effector molecules [41,42]. As self-protective mechanisms, CTLs express cell-surface cathepsins and intracellular serpin PI-9 to proteolytically degrade granzymes or inhibit their cleavage activity [20,43]. Although the release of effector molecules is directed to the immune synapse, extracellular GzmB can be readily detected using standardized assays such as ELISpot. Moreover cell-free GzmB levels have been used to monitor cytotoxic activity *in vivo* including cancer and rheumatoid arthritis [44,45]. Because our nanosensors are formulated to probe extracellular protease activity, we sought to quantify GzmB expression during T cell killing in both intracellular and extracellular spaces, and assess the ability of our nanosensors to detect anti-graft cytotoxicity ex vivo.

To validate that nanosensors are sensitive to physiologically relevant concentrations of GzmB, we utilized a T cell killing assay composed of transgenic OT1 T cells, which recognize the peptide epitope SIINFEKL from chicken ovalbumin (OVA), and target EG7-OVA or EL4 cells that express or lack the OVA antigen respectively [46]. We first verified intracellular expression of GzmB in activated OT1 T cells co-cultured with EG7-OVA target cells compared to EL4 controls (Supplemental Figure S6A, B). To confirm protease activity of GzmB, we used commercial fluorogenic probes that produce fluorescent signals after intracellular cleavage by GzmB in target cells. Whereas GzmB activity was not significantly elevated in EL4 target cells, significant GzmB activity was observed in EG7-OVA cells at T cell to target cell ratios of 1:1 and 10:1 (***P, n = 3, Figure 3A–C). To quantify the amount of GzmB secreted into the extracellular space, we analyzed co-culture supernatants by ELISA and detected an ~10-fold increase in GzmB between EG7-OVA and EL4 samples at a 10:1 ratio (****P, n = 3, Figure 3D), which indicated significant GzmB was released into the extracellular space. Under these co-culture parameters, we incubated fluorescently labelled nanosensors with conditioned supernatant and detected significant increases in

initial cleavage velocities (V_o) at an OT1 : EG7.OVA ratio of 10, which was consistent with the level of extracellular GzmB as quantified by ELISA (Figure 3E, F). In co-cultures containing equal number of OT1 T cells and EG7.OVA target cells, nanosensors were activated by secreted GzmB concentrations of ~1.7 pM (~50 pg/mL) (Figure 3D, F), which was several orders of magnitude lower than reported concentrations (100–500 nM) that have been used to induce *in vitro* target cell death [47–49]. These data confirmed that protease activity amplifies detection signals to allow our GzmB nanosensors to sense cytotoxic T cell activity. We next sought to further test the sensitivity of nanosensors against alloreactive T cells. To do so, we collected splenocytes and lymphocytes from recipient C57BL/6 mice that were either transplanted with skin allografts from major histocompatibility complex (MHC) mismatched BALB/c donor mice or isografts from donor C57BL/6 mice. Co-incubation of harvested allograft cells with BALB/c splenocytes and nanosensors resulted in significant increases in GzmB activity as monitored by sample fluorescence, which was not detected in samples co-cultured with T cells harvested from isograft mice (Figure 3G, H). These results showed that GzmB activity nanosensors detect alloreactive T cell killing activity.

Urinary pharmacokinetic switch enables remote detection

We next set out to establish the potential of using GzmB activity nanosensors to probe anti-graft T cell activity *in vivo*. During post-transplant tissue injury, damaged associated molecular patterns (DAMPs) trigger the release of proinflammatory cytokines (e.g., TNF-alpha, IL-6) by innate immune cells that increase local vessel permeability, blood flow, and immune cell infiltration [4,50,51]. By histopathology, classifications of early stage T cell rejection (Borderline TCMR, TCMR IA, and TCMR IB) all indicate interstitial inflammation as a defining feature [52]. Localized vasodilation enhances delivery and accumulation of nanomedicines to inflamed disease sites, as demonstrated by prior studies targeting atherosclerotic plaques and tumors [53–55]. To produce a diagnostic signal in urine, activity nanosensors are formulated with a nanoparticle core that functions to passively target allograft tissue and initiate a pharmacokinetic switch whereby surface substrates are cleaved by local GzmB activity and then traffic into urine for analysis. Thus, we sought to quantify the extent to which the components of our nanosensors (i.e., peptide and IONP) accumulate in inflamed allograft tissue as well as size-dependent trafficking of GzmB reporter signals to urine during rejection.

To assess IONP organ distribution, we intravenously (i.v.) administered surface-labeled IONPs to recipient C57BL/6 mice simultaneously transplanted with both skin allografts and isografts to directly compare targeting by full-body fluorescent imaging (Figure 4A). We found significant accumulation of nanosensors in allografts as early as postoperative day (POD) 3 compared to isograft controls. Preferential accumulation peaked on POD 7 with 4-fold signal increase over skin isograft (**P, n = 5) and was statistically equivalent by POD 9, which we attributed to tissue necrosis, scab formation, and vascular occlusion characteristic of late stage rejection of allografts (Figure 4A–B, Supplemental Figure S7). To assess biodistribution, we found higher levels of IONPs in organs with fenestrated endothelium (liver, spleen, lymph nodes) over others (brain, heart, kidney, lung) – which was consistent with the vast majority of nanomedicines [53,55] – and no significant differences across all organs between allograft and isograft cohorts of mice (Supplemental Figure S8). These

studies were performed post-mortem and did not allow direct quantification of IONPs in the bladder due to spontaneous voiding of urine resulting from the relaxation of urethral sphincter muscles. Therefore, we used live whole animal fluorescent imaging and found no accumulation of IONPs in the bladders of mice, which is consistent with the kidney size filtration limit (~ 5 nm) previously shown for inorganic nanomaterials [56] (Supplemental Figure S9A-C). To examine peptide pharmacokinetics, we administered free fluorophore-labeled GzmB substrates and found significant increases in perfusion in allograft tissue compared to isograft controls (*P, n = 3, Supplemental Figure S9D-F), but statistically equivalent clearance into urine between allograft and isograft bearing animals (Supplemental Figure S9G, H). These data showed that free IONPs and GzmB substrates accumulate in allograft tissue.

Next, to investigate the sites of GzmB activation *in vivo*, we designed an activatable probe where the fluorophore is proximal to the IONP surface and remains attached after cleavage while the quencher is released (Figure 4C). This design prevents fluorescent signals from being washed away and allows tissue localization of fluorescent IONPs. We first verified probe activation *in vitro* by recombinant GzmB (Supplemental Figure S10A-C), and *in vivo*, found that probe activation was significantly increased in allograft skin but statistically equivalent in all major organs (****P, n = 5, Figure 4D, Supplemental Figure S11). To visualize peptide cleavage and trafficking of fluorescent reporter fragments into urine, we infused IONPs conjugated with homoquenched GzmB substrates (Supplemental Figure S12) and analyzed major organs by fluorescent imaging (Figure 4E). In allograft mice, we found 3-fold higher fluorescence in kidneys compared to isograft mice (****P, n= 4–5, Figure 4F, Supplemental Figure S13), which we attributed to active renal filtration of cleaved peptide fragments. This observation was further supported in live animal imaging where we observed increases in fluorescent signals in bladders of allograft mice (Figure 4G). Collectively, our data showed that GzmB activity nanosensors preferentially accumulate and activate in allograft tissue during rejection, and after cleavage, peptide fragments are efficiently cleared into host urine.

Noninvasive and early detection of ACR

Histological criteria for staging severity of ACR include features, such as tissue damage and presence of apoptotic cells [57], which are downstream effects of anti-graft T cell responses. Activity measurements of proteases that drive disease pathology have the potential to be early biomarkers and anticipate disease trajectory, such as using (Matrix metalloproteinases) MMP activity to predict liver fibrosis progression and regression [27,28]. We therefore investigated the potential of using GzmB activity nanosensors for early detection of ACR (Figure 5A). To quantify skin graft health and rejection kinetics, we assigned a score of 4 for healthy allografts, a score of 0 for full rejection, and intermediate scores based on features such as the ratio of viable to necrotic skin and the presence of ulcerations or scabs. According to these metrics, graft scores began to significantly decrease at day 9 after transplant (2.5 vs. 3.9, ****P; Figure 5B, C and Supplemental Figure S14) and reached endpoint when allografts were completely rejected within two weeks post-transplant. To identify the earliest timepoint of GzmB upregulation, we analyzed activated CD8 T cells from spleens and draining lymph nodes at day 5, 7 and 9. While GzmB levels at day 5 were

unchanged compared to controls, we detected an increase in the frequency of GzmB expressing CD8 T cells in allograft animals by day 7 (Supplemental Figure S15) when graft scores remained statistically equivalent between allograft and isograft tissues. To support our findings, we analyzed graft tissue on day 7 by immunohistochemistry and found significant increases in both graft-infiltrating CD8 T cells and GzmB expression levels (Figure 5D–G). Taken together, our data provided evidence that GzmB levels were significantly upregulated in allograft tissue at the onset of acute rejection.

To determine conditions for serial monitoring, we first evaluated the immunogenicity of our formulation and found that GzmB peptides or nanosensors do not induce neutralizing antibodies when co-injected with or without complete Freud's adjuvant (Supplemental Figure S16). Moreover, we analyzed residual urinary fluorescence from a single injection and found full clearance within 2 days after administration (Supplemental Figure S17). Based on these results, we sought to determine how early our system can detect the onset of ACR by administering nanosensors and performing urinalysis in transplanted mice before (POD −4) and at early PODs separated by 2 days (PODs 3, 5, and 7). Using pre-graft urine signals as baseline for recipients, we did not detect significant elevations in post-graft urine signals from naïve, isograft, and CD8 depleted control cohorts of mice (Figure 5H; Supplemental Figure S18A, B). By contrast, post-graft urine signals from allograft recipients were significantly elevated as early as POD 5 (**P, n = 6) and further increased by POD 7 (****P, n = 6, Figure 5H), detecting GzmB activity several days before graft scores were statistically significant between allo and isografts (Figure 5C). To assess sensitivity and specificity, we analyzed urine signals by receiver-operating-characteristic (ROC) analysis and quantified an increase in AUROC from 0.67 to 0.98 by POD 7 (95% confidence interval of 0.94 to 1.03). Altogether, these results illustrated that systemic administration of GzmB activity nanosensors in allograft recipients produce urine signals that classify ACR with high sensitivity and specificity.

The use of immunosuppressive drugs as maintenance therapy has significantly reduced the rates of ACR; however, rejection episodes may occur despite ongoing immunosuppression or in patients treated with subtherapeutic doses [58,59]. To assess the sensitivity of this approach to detect T cell activity under immunosuppression, we performed urinalysis of allograft-bearing mice treated with the calcineurin inhibitor (CNI) Tacrolimus which directly inhibits downstream calcium-dependent signaling events in T cells (Figure 6A). Daily treatment with high-dose Tacrolimus (2 mg/kg) improved skin allograft outcome as quantified by both graft scores and survival curves, but was subtherapeutic and did not prevent eventual graft loss due to MHC-mismatched donor and recipient mice (Figures 6B, C). Compared to pre-graft urine signals on POD −4 (Figure 6D, Supplemental Figure S19), post-graft urine signals were significantly elevated on POD 7 (*P, n = 6) and POD 12 (**P, n = 6), which indicated elevated GzmB activity in recipient mice under subtherapeutic immunosuppression. However, as anticipated by direct inhibition of T cell activity with CNIs, urine signals from treated mice were blunted compared to untreated mice (Figure 6E). These results showed that our urine measurements are sensitive to GzmB activity under subtherapeutic immunosuppression and provide an early indicator of eventual graft failure.

Discussion

The invasive core biopsy is considered the “gold” standard for diagnosing ACR; however, it is associated with significant patient morbidity, sampling variability, and provides a static snapshot of anti-graft activity [7,8]. Here, we developed GzmB activity nanosensors, consisting of an IONP core decorated with peptide substrates, to sense CD8 T cell killing. In a skin graft mouse model of ACR, these nanosensors accumulate in allograft tissue and are cleaved locally by GzmB, which then triggers a pharmacokinetic switch to enable detection of peptide fragments from recipient urine. Our nanosensors noninvasively detect the onset of ACR with high sensitivity and specificity, and in allograft mice under subtherapeutic immunosuppression, produce urine signals that precede eventual graft failure.

The use of a nanoparticle carrier increases circulation half-life of substrate peptides, which are otherwise cleared from the body by renal filtration within minutes after i.v. administration [32]. Without conjugating peptides to a nanoscale scaffold larger than the glomerulus pore size of ~ 5 nm [60], urine samples would otherwise be confounded with uncleaved peptide substrates. We selected IONPs because they are FDA-approved and well-tolerated in humans [33], but alternative formulations with different carriers (e.g., PEG, dextran) can be used to tune pharmacokinetics [30]. Here we leveraged graft inflammation during early ACR [52,61,62] to passively deliver nanosensors. Because skin transplants are initially avascular, we anticipate that passive targeting may be enhanced for vascularized solid transplants (e.g., kidney, liver, heart), particularly for organs with porous, fenestrated endothelium such as the liver. Given the wealth of targeting and delivery strategies in nanomedicine, this system will be amenable to functionalization with organ-specific or inflammation targeting ligands [63,64] to direct delivery to specific anatomical sites or enhance diagnostic signals [65].

Our study focused on GzmB activity as an early biomarker for ACR. Clinical studies have shown that increased expression of GzmB is found in allograft tissue during Banff TCRM IA and IB, precedes progression to grade II or higher, and has the potential to predict graft outcomes [13,14,17,19,66]. To measure protease activity *in vivo*, existing activity-based sensors are designed to produce a localized fluorescent signal, which is subject to tissue scattering and washout by blood that attenuates the strength of the detection signal [21,67–70]. By contrast, our technology is based on local cleavage and remote detection of cleaved reporters enriched in urine, which amplifies detection signals to increase the sensitivity to early stage analysis. Noninvasive biomarkers that rely on shed molecules or the contents of dead cells [10,11] experience significant dilution in blood and may be limited for early stage detection [71,72]. While the performance of this method for ACR detection in a preclinical setting (AUROC = 0.98) compares favorably to other biomarkers, such as serum creatinine (0.63), NGAL (0.6–0.9), KIM-1 (0.8), and Cystatin C (0.64–0.82) [73–76], the translation of this approach will require rigorous evaluation in humans and guidance by regulatory and community qualifications[77].

The use of calcineurin inhibitors such as Tacrolimus is closely monitored in patients to maintain graft tolerance and target blood concentrations [78]. In our study, the Tacrolimus dose was subtherapeutic despite administration at doses (2 mg/kg) 20–200 fold higher

compared to patients, and did not prevent eventual graft loss in mice. This discrepancy in dose results from the use of MHC-mismatched donor and recipients in skin graft models to allow ACR to occur within a reasonable experimental window (~7–10 days). In humans, donor and recipient MHC matching allows lower effective concentrations of CNIs to induce and maintain graft tolerance. Our study showed that urine measurements of GzmB activity anticipated eventual graft failure in mice under sub-therapeutic immunosuppression, which may allow for dose adjustment or additional therapeutic interventions in patients.

In future, this technology will benefit by expanding our single GzmB probe into a family of nanosensors designed to sense different proteases, which can be accomplished by the use of mass barcodes that uniquely label each peptide substrate for multiplexed quantification by mass spectrometry [27]. We anticipate that a family of activity sensors against a panel of proteases (e.g., T cell, fibrosis, and viral proteases) will allow staging of ACR and discrimination between different injuries that likewise depend on CD8 T cell cytotoxicity. These include the ability to differentially diagnose anti-graft from anti-viral activity (e.g., BK, CMV, HCV) that occurs with high prevalence in transplant patients [79]. The expanded library may also include proteases from the complement cascade to allow monitoring of antibody-mediated rejection (AMR), which is responsible for the majority of long-term graft loss [80], or organ-specific proteases (e.g. liver protease hepsin) for signal normalization. These improvements may provide the capacity to differentiate ACR from AMR with high diagnostic power, and resolve anti-graft activity into the relative contributions of each mechanism to personalize management of transplant recipients.

Methods

Animals

6- to 8-week old male mice were used at the outset of all experiments. OT1 transgenic mice (C57BL/6-Tg(TcraTcrb)1100Mjb/J) were purchased from Jackson Laboratories. C57BL/6 and BALB/c mice for skin graft experiments and CFW control mice were purchased from Charles River Laboratories. All animal protocols were approved by Georgia Tech IACUC (protocol #A14100) and Emory University IACUC (protocol #DAR-2002797–082117GN). All authors have complied with relevant ethical regulations while conducting this study.

Nanosensor synthesis and characterization

Aminated IONPs were synthesized in house per published protocol [35]. FITC-labelled GzmB substrate peptides ((FITC)AIEFDSGc; lower case letters = d-form amino acids) were synthesized by Tufts University Core Facility and used for in vivo formulation. FITC-labelled GzmB substrate peptides with internal quencher ((5-FAM)aIEFDSGK(CPQ2)kkc) were synthesized by CPC Scientific and used for all in vitro activity assays. Aminated IONPs were first reacted to the heterobifunctional crosslinker Succinimidyl Iodoacetate (SIA; Thermo) for 2 hours at room temperature (RT) and excess SIA were removed by buffer exchange using Amicon spin filter (30 kDa, Millipore). Sulfhydryl-terminated peptides and Polyethylene Glycol (PEG; LaysanBio, M-SH-20K) were mixed with NP-SIA (90:20:1 molar ratio) and reacted overnight at RT in the dark to obtain fully conjugated activity nanosensors. Activity nanosensors were purified on a Superdex 200 Increase 10–300

GL column using AKTA Pure FPLC System (GE Health Care). Ratios of FITC per IONP were determined using absorbance of FITC (488 nm, ε = 78,000 $cm^{-1}M^{-1}$) and IONP (400 nm, ε = 2.07 × 10^6 $cm^{-1}M^{-1}$)[35,81] measured with Cytation 5 Plate Reader (Biotek). At this conjugation condition, our resulting formulations have an average of 50 FITC-labelled peptides per nanoparticle core. DLS measurements of activity nanosensors were done in PBS or mouse plasma at RT using Zetasizer Nano ZS (Malvern).

In vitro protease cleavage assays

Activity nanosensors (6 nM by NP, 300 nM by peptide) were incubated in PBS + 1% bovine serum albumin (BSA; Sigma) at 37 °C with murine Granzyme B (0.17 μM; Peprotech), human thrombin (13.5 μM; HaemTech), mouse thrombin (12.5 μM; HaemTech), mouse plasmin (2.94 μM; HaemTech), C1r (1.43 μM; Sigma), C1s (1.80 μM; Sigma), Factor D (0.20 μM; Sigma), Factor I (0.79 μM; Sigma), MASP2 (0.08 μM; Biomatik). Sample fluorescence were measured for 60 minutes using Cytation 5 plate reader (Biotek). To optimize GzmB substrate, a library of potential substrates was synthesized by Tufts University Core Facility peptide synthesis service and conjugated to IONPs. Cleavage assays of nanoparticles decorated with these substrates with recombinant GzmB were performed, and data was fitted to compare initial cleavage velocities. To determine Michaelis-Menten constants, cleavage assays with GzmB were performed at different substrate concentrations. To initiate coagulation cascade, citrated plasma was mixed with activity nanosensors before addition of calcium chloride (15 mM, Sigma). To initiate complement activation, Control Human Serum (Sigma) was mixed with activity nanosensors before addition of Heat Aggregated Gamma Globulin (HAGG; Quidel) per the manufacturer's protocol. After measuring fluorescence for 1 hour, supernatants were collected and measured for formation of MAC complex using MicroVue CH50 Eq EIA Kit (Quidel).

GzmB characterization in transgenic T cell cocultures

EL4 and EG7-OVA cells (ATCC) were grown in RPMI 1640 supplemented with 10% FBS and 25mM HEPES (Gibco). EG7-OVA cultures were supplemented with G418 (0.4 mg/ml, InvitroGen). CD8 T cells were isolated from OT1 (Jackson Labs) splenocytes by MACS using CD8a Microbeads (Miltenyi). Cells were activated by seeding in 96-well plates pre-coated with anti-mouse CD3e (1 μg/ml working concentration, Clone: 145–2C11, BD) and anti-mouse CD28 (2 μg/ml working concentration, Clone: 37.51, BD) at 2×10^6 cells/ml in RPMI 1640 supplemented with 10% FBS, 100U/ml penicillin-streptomycin, 1X non-essential amino acids (Gibco), 1mM sodium pyruvate, 0.05mM 2-mercaptoethanol, and 30U/ml hIL-2 (Roche). After 2 days, cells were washed and transferred to uncoated plates. On day 5, 1 × 10^6 activated OT1 T cells were coincubated with 1×10^6 EL4 or EG7-OVA cells for 2 hours at 37 °C and stained for GzmB using anti-mouse GzmB (Clone: NGZB, eBioScience) and Intracellular Fixation & Permeabilization Buffer Set (eBioScience, 88–8824-00). To measure GzmB activity inside target cells, we coincubated activated OT1 CD8 T cells with EL4 and EG7-OVA target cells at various T cell to target cell ratios and stained using GranToxiLux Kit (OncoImmunin, GTL702–8). To measure secretory GzmB, we collected coculture supernatant of OT1 with target cells and performed ELISA with Granzyme B Mouse ELISA Kit (eBioScience, BMS6029).

Nanosensor assay sensing T cell killing

To sense transgenic T cell killing, CD8+ OT1 T cells were isolated and activated per above protocol. On day 5 post activation, 1×10^5 OT1 T cells were coincubated with 1×10^5 EL4 or EG7-OVA target cells for 2 hours at 37 °C. Coculture supernatants were mixed with activity nanosensors (2 nM by NP, 100 nM by peptides) and fluorescence were monitored for 1 hour at 37 °C. To sense alloreactive T cell killing, on POD 7, CD8 T cells were isolated from splenocytes and lymphocytes of skin graft mice. 5×10^5 CD8 T cells from skin graft mice were restimulated with 5×10^5 splenocytes from BALB/c Mice (Charles River) for 6 hours at 37 °C. Coculture supernatants were mixed with activity nanosensors (2 nM by NP, 100 nM by peptides) and fluorescence were monitored for 2 hours at 37 °C.

Skin graft surgery

Recipient C57BL/6 animals (Charles River) were administered i.p. an anesthetic cocktail of ketamine (100 mg/Kg; GT PRL) and xylazine (100 mg/Kg; GT PRL) followed by sustained-released buprenorphine (1mg/kg, i.p.; GT PRL) right before surgery. The hair was shaved from the upper lateral thoracic walls of the recipient animal prior to surgery. The surgical site was cleaned 3 times, alternating between isopropyl alcohol (GT PRL) and chlorhexidine (GT PRL). Donor BALB/c or C57BL/6 animals (Charles River) were euthanized under isoflurane sedation by cervical dislocation. Segments of tail skin (each approximately ~1 cm^2) was be removed from the donor animals and kept in sterile saline on ice until the grafting procedure. In recipient C57BL/6 mice, the skin on the lateral thoracic walls was be removed using surgical scissors, to created similarly sized defects compared to the segment of tail skin. The donor skin was then placed over the site to cover the wound defect. The site was protected by wrapping a commercial bandage (“band-aid”) that covers the graft site and firmly wrapped around the body of the animal.

Skin graft scoring and survival analysis

Skin grafts were qualitatively scored on a scale ranging from 0–4 per established protocol by the Emory Transplant Center. Scoring involved direct observation and palpation of the graft and surrounding tissue. A score of 4 is for a perfect-appearing skin graft. If donor was of BALB/c origin, the grafted skin with a score of 4 will be light pink and slightly velvety. Hair can be seen growing from the graft. No imperfection is noted. A score of 3 is for grafts which are good but not perfect in appearance, such as a graft which might otherwise merit a 4 but for a single red ulcer comprising less than 25% of the graft area. Other reasons for a score of 3 might be faint scabbiness over the ear skin graft or slight hardening at the edges of a tail skin graft. A score of 2 is given for grafts which are half necrotic. For example, half of the graft area may be covered by red ulcers or scaly, red, and thickened skin, but half of the graft still consists of viable skin. Grafts which have shrunk to 50% of their original size receive a score of 2. A score of 1 is given for grafts which are nearly completely necrotic but which still have some small areas of viable skin. Grafts with a score of 1 will typically be totally necrotic within one week. A score of 0 is given when a graft has been fully rejected and the transplanted skin is completely necrotic. For Kaplan-Meier survival analysis, a skin graft was considered rejected when its score was below 1.

Measurement of circulation half-life

For all half-life characterization, VT750 labelled nanosensors (20 μg by mass, 10 nmol by peptide) or peptides (10 nmol) were administered i.v. to control CFW mice (Charles River). At several time points following administration, blood was collected into heparin-coated Capillary Tubes (VWR) via retro-orbital collection and imaged using Odyssey CLx Imaging System (LI-COR). A ladder with known concentrations of NIR dye was imaged at the same time to correlate sample fluorescence to dye concentrations.

Pharmacokinetic studies

Mice bearing skin grafts were administered with nanosensors (20 μg) or peptides (10 nmol) labelled with VivoTag S-750 (VT750; PerkinElmer). Nanosensors and peptides were labeled with VT750 (3:1 molar ratio) using NHS chemistry per manufacturer's protocol. For organ biodistribution, whole mice were imaged with IVIS Spectrum CT Imaging System (PerkinElmer) while excised organs were imaged with Odyssey CLx Imaging System (LI-COR) 24 hours after administration. For urine pharmacokinetics, whole mice were imaged with IVIS Spectrum CT Imaging System (PerkinElmer) at 90 minutes post administration. To track cleaved fragments after in vivo GzmB cleavage, on day 7 post-transplant, VT750-labelled activity nanosensors (10 nmol by peptides) were administered to skin graft mice. At 90-minute post administration, whole mouse was imaged with IVIS Spectrum CT Imaging System (PerkinElmer) to analyze the extend of fluorescence from the bladder. Major organs were then excised and homogenized using Lysing Matrix A Tubes and FastPrep24 Homogenizer (MP Biomedicals). Tissue homogenates were transferred to a 96-well plate and then imaged with Odyssey CLx Imaging System (LI-COR).

GzmB activity imaging

GzmB substrate peptides with non-natural amino acids for manual labelling (kGGsIEFDSGGGs{PRA}c) was purchased from Genscript. After the peptides were coupled to IONPs, the NIR dye IRDye-800CW (LICOR) was couple to L-propargylglycine ({PRA}) via copper catalyzed click chemistry[82]. The NIR quencher was then coupled to the N-terminal Lysine via traditional NHS chemistry according to the manufacturer's protocol to generate the NIR GzmB activity probes. The extent of successful quenching and enzymatic activation were analyzed *in vitro* by absorbance analysis and LICOR imaging upon addition of recombinant GzmB (Peprotech). For *in vivo* GzmB activity imaging study, NIR GzmB activity probes (10 nmol by peptide) were administered to skin graft mice. Major organs were excised at 24 hours and imaged with Odyssey CLx Imaging System (LICOR).

GzmB characterization in skin graft mouse model

For histological analysis, tissues were collected from skin graft mice on POD 7. All tissues were fixed in 4% paraformaldehyde (EMS) overnight at 4°C, washed 3 times with PBS and stored in 70% ethanol (VWR) until paraffin-embedding, sectioning, and staining for GzmB and CD8 (Winship Pathology Core). For flow cytometry analysis, 1×10^6 splenocytes or lymphocytes isolated from skin graft mice on PODs 5, 7, and 9 were restimulated with 1×10^6 BALB/c splenocytes for 6 hours at 37 °C before staining for GzmB using anti-mouse

GzmB (Clone: NGZB, eBioScience) and Intracellular Fixation & Permeabilization Buffer Set (eBioScience).

Urinary prediction of acute rejection in skin graft mice

All urinalysis experiments were done in paired setup. Before (POD −4) and at various time points after transplantation, skin graft mice were administered with FITC-labelled activity nanosensors (10 nmol by peptides). Mice were placed over 96-well polystyrene plates surrounded by an open cylindrical sleeve covered by a weighted petri dish to prevent animals from jumping out of the cylinder. Animals were left to urinate for 90 minutes before urine samples were collected. FITC in urine was purified by a magnetic separation assay using Dynabeads (Thermo, 65501) coated with anti-FITC antibody (GeneTex, GTX10257) according to manufacturer's protocol. Fluorescent signals were measured with Cytation 5 Plate Reader (Biotek). Concentrations of FITC from urine samples were calculated using a free FITC ladder and normalized with urine volume to obtain percent injected dose. To account for batch-to-batch differences in nanosensors, the percent of injected dose is normalized by the average and variance to pre-transplant signals and plotted as normalized urine fluorescence.

In vivo CD8 T cell depletion

For CD8 depletion study, mice were given anti-mouse CD8 (clone: 53–6.7, BioXCell) for 3 consecutive days following with booster shots every 3 days after. Flow cytometry analysis of splenocytes and lymphocytes were performed with anti-mouse CD3 (clone: 17A2, Biolegend), anti-mouse CD4 (clone: RM4–5, Biolegend), anti-mouse CD8 (clone: KT15, Serotec) to confirm success of depletion.

Administration of immunosuppression

For drug response study, allograft mice were given either tacrolimus (2 mg/Kg, I.P.; Prograft®) or saline every day starting from POD −1 until POD 7. Mice were given two more injections on PODs 9 and 11.

Immunogenicity study

On POD 0, C57BL/6 mice were inoculated I.P. with 200 μL of GzmB peptide (10 nmol), GzmB nanosensors (10 nmol by peptide), GzmB nanosensors (10 nmol by peptide, 100 μL) + Complete Freund's Adjuvant (CFA, 100 μL; Sigma), chicken ovalbumin (100 μg, 100 μL; Sigma) + CFA (100 μg), and saline. Blood was collected via retroorbital blood draw into serum collection tube (CAPIJECT) and centrifugated for 5 min at 3,500 G. Serum samples were collected and stored at −80°C until analysis. Total IgG levels in serum was determined using Easy-Titer™ Mouse IgG Assay Kit (Thermo).

Software and Statistical Analysis

Graphs were plotted and appropriate statistical analyses were conducted using GraphPad Prism (*P< 0.05, **P < 0.01, ***P < 0.001, ****P < 0.0001; central values depict the means, and error bars depict s.e.m.). Quantification of histological images was performed on ImageJ (NIH). Whole-mouse fluorescent data were analyzed using Living Image

(PerkinElmer). Whole-organ fluorescent data were analyzed using Image Studio (LI-COR). Flow cytometry data were analyzed using FlowJo X (FlowJo, LLC). Power analyses were performed using G*Power 3.1 (HHUD).

Supplementary Material

Refer to Web version on PubMed Central for supplementary material.

Acknowledgments

This work was funded by an NIH Director's New Innovator Award DP2HD091793 awarded to G.A.K. and National Institutes of Health U01 AI132904 awarded to A.B.A. Q.D.M. is supported by the NSF Graduate Research Fellowships Program (Grant No. DGE-1650044). D.V.M. is supported by National Institutes of Health F30 award number DK109665. B.A.H is supported by the National Institutes of Health GT BioMAT Training Grant under Award Number 5T32EB006343. G.A.K. holds a Career Award at the Scientific Interface from the Burroughs Wellcome Fund. The content is solely the responsibility of the authors and does not necessarily represent the official views of the National Institutes of Health.

References

1. Mas VR, Mueller TF, Archer KJ & Maluf DG Identifying biomarkers as diagnostic tools in kidney transplantation. Expert Rev. Mol. Diagn 11, 183–196 (2011). [PubMed: 21405969]
2. Gwinner W Renal transplant rejection markers. World J. Urol 25, 445 (2007). [PubMed: 17786452]
3. Cornell LD, Smith RN & Colvin RB Kidney Transplantation: Mechanisms of Rejection and Acceptance. Annu. Rev. Pathol. Mech. Dis 3, 189–220 (2008).
4. Nankivell BJ & Alexander SI Rejection of the Kidney Allograft. N. Engl. J. Med 363, 1451–1462 (2010). [PubMed: 20925547]
5. Sijpkens YWJ et al. Early versus late acute rejection episodes in renal transplantation. Transplantation 75, 204 (2003). [PubMed: 12548124]
6. Moreau A, Varey E, Anegon I & Cuturi M-C Effector Mechanisms of Rejection. Cold Spring Harb. Perspect. Med 3, (2013).
7. Furness PN, Taub N & Convergence of European Renal Transplant Pathology Assessment Procedures (CERTPAP) Project. International variation in the interpretation of renal transplant biopsies: report of the CERTPAP Project. Kidney Int 60, 1998–2012 (2001). [PubMed: 11703620]
8. Piovesan AC et al. Multifocal renal allograft biopsy: impact on therapeutic decisions. Transplant. Proc 40, 3397–3400 (2008). [PubMed: 19100398]
9. Jaffa MA et al. Analyses of renal outcome following transplantation adjusting for informative right censoring and demographic factors: A longitudinal study. Ren. Fail 32, 691–698 (2010). [PubMed: 20540637]
10. Josephson MA Monitoring and Managing Graft Health in the Kidney Transplant Recipient. Clin. J. Am. Soc. Nephrol 6, 1774–1780 (2011). [PubMed: 21734093]
11. Vlaminck ID et al. Circulating Cell-Free DNA Enables Noninvasive Diagnosis of Heart Transplant Rejection. Sci. Transl. Med 6, 241ra77–241ra77 (2014).
12. Choy JC Granzymes and perforin in solid organ transplant rejection. Cell Death Differ 17, 567–576 (2010). [PubMed: 19876069]
13. Wagrowska-Danilewicz M & Danilewicz M Immunoexpression of perforin and granzyme B on infiltrating lymphocytes in human renal acute allograft rejection. Nefrol. Publicacion Of. Soc. Espanola Nefrol 23, 538–544 (2003).
14. Rowshani AT et al. Hyperexpression of the granzyme B inhibitor PI-9 in human renal allografts: A potential mechanism for stable renal function in patients with subclinical rejection. Kidney Int 66, 1417–1422 (2004). [PubMed: 15458434]
15. Kummer JA et al. Expression of granzyme A and B proteins by cytotoxic lymphocytes involved in acute renal allograft rejection. Kidney Int 47, 70–77 (1995). [PubMed: 7731173]

16. Suthanthiran M et al. Urinary-Cell mRNA Profile and Acute Cellular Rejection in Kidney Allografts. N. Engl. J. Med 369, 20–31 (2013). [PubMed: 23822777]
17. Simon T, Opelz G, Wiesel M, Ott RC & Süsal C Serial peripheral blood perforin and granzyme B gene expression measurements for prediction of acute rejection in kidney graft recipients. Am. J. Transplant. Off. J. Am. Soc. Transplant. Am. Soc. Transpl. Surg 3, 1121–1127 (2003).
18. Calafiore R & Basta G Clinical application of microencapsulated islets: Actual prospectives on progress and challenges. Adv. Drug Deliv. Rev 67–68, 84–92 (2014).
19. Li B et al. Noninvasive diagnosis of renal-allograft rejection by measurement of messenger RNA for perforin and granzyme B in urine. N. Engl. J. Med 344, 947–954 (2001). [PubMed: 11274620]
20. Sun J et al. A cytosolic granzyme B inhibitor related to the viral apoptotic regulator cytokine response modifier A is present in cytotoxic lymphocytes. J. Biol. Chem 271, 27802–27809 (1996). [PubMed: 8910377]
21. Edgington LE, Verdoes M & Bogyo M Functional imaging of proteases: recent advances in the design and application of substrate-based and activity-based probes. Curr. Opin. Chem. Biol 15, 798–805 (2011). [PubMed: 22098719]
22. Sanman LE & Bogyo M Activity-Based Profiling of Proteases. Annu. Rev. Biochem 83, 249–273 (2014). [PubMed: 24905783]
23. Konishi M et al. Imaging Granzyme B Activity Assesses Immune-Mediated MyocarditisNovelty and Significance. Circ. Res 117, 502–512 (2015). [PubMed: 26199323]
24. Larimer BM et al. Granzyme B PET Imaging as a Predictive Biomarker of Immunotherapy Response. Cancer Res 77, 2318–2327 (2017). [PubMed: 28461564]
25. Whitley MJ et al. A mouse-human phase 1 co-clinical trial of a protease-activated fluorescent probe for imaging cancer. Sci. Transl. Med 8, 320ra4–320ra4 (2016).
26. Olson ES et al. In vivo fluorescence imaging of atherosclerotic plaques with activatable cell-penetrating peptides targeting thrombin activity. Integr. Biol. Quant. Biosci. Nano Macro 4, 595–605 (2012).
27. Kwong GA et al. Mass-encoded synthetic biomarkers for multiplexed urinary monitoring of disease. Nat. Biotechnol 31, 63–70 (2013). [PubMed: 23242163]
28. Lin KY, Kwong GA, Warren AD, Wood DK & Bhatia SN Nanoparticles That Sense Thrombin Activity As Synthetic Urinary Biomarkers of Thrombosis. ACS Nano 7, 9001–9009 (2013). [PubMed: 24015809]
29. Warren AD, Kwong GA, Wood DK, Lin KY & Bhatia SN Point-of-care diagnostics for noncommunicable diseases using synthetic urinary biomarkers and paper microfluidics. Proc. Natl. Acad. Sci 111, 3671–3676 (2014). [PubMed: 24567404]
30. Kwong GA et al. Mathematical framework for activity-based cancer biomarkers. Proc. Natl. Acad. Sci 112, 12627–12632 (2015). [PubMed: 26417077]
31. Holt BA, Mac QD & Kwong GA Nanosensors to Detect Protease Activity In Vivo for Noninvasive Diagnostics. J. Vis. Exp (2018). doi:10.3791/57937
32. Fosgerau K & Hoffmann T Peptide therapeutics: current status and future directions. Drug Discov. Today 20, 122–128 (2015). [PubMed: 25450771]
33. Anselmo AC & Mitragotri S Nanoparticles in the clinic. Bioeng. Transl. Med 1, 10–29 (2016). [PubMed: 29313004]
34. Arami H, Khandhar A, Liggitt D & Krishnan KM In vivo delivery, pharmacokinetics, biodistribution and toxicity of iron oxide nanoparticles. Chem Soc Rev 44, 8576–8607 (2015). [PubMed: 26390044]
35. Park J-H et al. Magnetic Iron Oxide Nanoworms for Tumor Targeting and Imaging. Adv. Mater 20, 1630–1635 (2008). [PubMed: 21687830]
36. Jokerst JV, Lobovkina T, Zare RN & Gambhir SS Nanoparticle PEGylation for imaging and therapy. Nanomed. 6, 715–728 (2011).
37. Harris JL, Peterson EP, Hudig D, Thornberry NA & Craik CS Definition and Redesign of the Extended Substrate Specificity of Granzyme B. J. Biol. Chem 273, 27364–27373 (1998). [PubMed: 9765264]

38. Waugh SM, Harris JL, Fletterick R & Craik CS The structure of the pro-apoptotic protease granzyme B reveals the molecular determinants of its specificity. Nat. Struct. Mol. Biol 7, 762–765 (2000).
39. Ruggles SW, Fletterick RJ & Craik CS Characterization of Structural Determinants of Granzyme B Reveals Potent Mediators of Extended Substrate Specificity. J. Biol. Chem 279, 30751–30759 (2004). [PubMed: 15123647]
40. Casciola-Rosen L et al. Mouse and Human Granzyme B Have Distinct Tetrapeptide Specificities and Abilities to Recruit the Bid Pathway. J. Biol. Chem 282, 4545–4552 (2007). [PubMed: 17179148]
41. Huppa JB & Davis MM T-cell-antigen recognition and the immunological synapse. Nat. Rev. Immunol 3, 973 (2003). [PubMed: 14647479]
42. Dustin ML & Long EO Cytotoxic immunological synapses. Immunol. Rev 235, 24–34 (2010). [PubMed: 20536553]
43. Balaji KN, Schaschke N, Machleidt W, Catalfamo M & Henkart PA Surface cathepsin B protects cytotoxic lymphocytes from self-destruction after degranulation. J. Exp. Med 196, 493–503 (2002). [PubMed: 12186841]
44. Locke FL et al. Phase 1 Results of ZUMA-1: A Multicenter Study of KTE-C19 Anti-CD19 CAR T Cell Therapy in Refractory Aggressive Lymphoma. Mol. Ther 25, 285–295 (2017). [PubMed: 28129122]
45. Goldbach-Mansky R et al. Raised granzyme B levels are associated with erosions in patients with early rheumatoid factor positive rheumatoid arthritis. Ann. Rheum. Dis 64, 715–721 (2005). [PubMed: 15471892]
46. Clarke S. Rm. et al. Characterization of the ovalbumin-specific TCR transgenic line OT-I: MHC elements for positive and negative selection. Immunol. Cell Biol 78, 110–117 (2000). [PubMed: 10762410]
47. Kurschus FC, Fellows E, Stegmann E & Jenne DE Granzyme B delivery via perforin is restricted by size, but not by heparan sulfate-dependent endocytosis. Proc. Natl. Acad. Sci 105, 13799–13804 (2008). [PubMed: 18772390]
48. Adrain C, Duriez PJ, Brumatti G, Delivani P & Martin SJ The Cytotoxic Lymphocyte Protease, Granzyme B, Targets the Cytoskeleton and Perturbs Microtubule Polymerization Dynamics. J. Biol. Chem 281, 8118–8125 (2006). [PubMed: 16415351]
49. Giesübel U, Dälken B, Mahmud H & Wels WS Cell binding, internalization and cytotoxic activity of human granzyme B expressed in the yeast *Pichia pastoris*. Biochem. J 394, 563–573 (2006). [PubMed: 16336214]
50. Mori DN, Kreisel D, Fullerton JN, Gilroy DW & Goldstein DR Inflammatory triggers of acute rejection of organ allografts. Immunol. Rev 258, 132–144 (2014). [PubMed: 24517430]
51. LaRosa DF, Rahman AH & Turka LA The Innate Immune System in Allograft Rejection and Tolerance. J. Immunol. Baltim. Md 1950 178, 7503–7509 (2007).
52. Haas M et al. The Banff 2017 Kidney Meeting Report: Revised diagnostic criteria for chronic active T cell–mediated rejection, antibody-mediated rejection, and prospects for integrative endpoints for next-generation clinical trials. Am. J. Transplant 18, 293–307
53. Maeda H, Wu J, Sawa T, Matsumura Y & Hori K Tumor vascular permeability and the EPR effect in macromolecular therapeutics: a review. J. Control. Release Off. J. Control. Release Soc 65, 271–284 (2000).
54. Fredman G et al. Targeted nanoparticles containing the proresolving peptide Ac2–26 protect against advanced atherosclerosis in hypercholesterolemic mice. Sci. Transl. Med 7, 275ra20 (2015).
55. Wilhelm S et al. Analysis of nanoparticle delivery to tumours. Nat. Rev. Mater 1, 16014 (2016).
56. Choi HS et al. Renal Clearance of Nanoparticles. Nat. Biotechnol 25, 1165–1170 (2007). [PubMed: 17891134]
57. Loupy A et al. The Banff 2015 Kidney Meeting Report: Current Challenges in Rejection Classification and Prospects for Adopting Molecular Pathology. Am. J. Transplant 17, 28–41 (2017). [PubMed: 27862883]

58. Vincenti F, Jensik SC, Filo RS, Miller J & Pirsch J A long-term comparison of tacrolimus (FK506) and cyclosporine in kidney transplantation: Evidence for improved allograft survival at five years. Transplantation 73, 775–782 (2002). [PubMed: 11907427]
59. Vincenti F et al. Belatacept and Long-Term Outcomes in Kidney Transplantation. N. Engl. J. Med 374, 333–343 (2016). [PubMed: 26816011]
60. Jeansson M & Haraldsson B Glomerular Size and Charge Selectivity in the Mouse after Exposure to Glucosaminoglycan-Degrading Enzymes. J. Am. Soc. Nephrol 14, 1756–1765 (2003). [PubMed: 12819235]
61. Hsauyry P et al. The Inflammatory Mechanisms of Allograft Rejection. Immunol. Rev 77, 85–142 [PubMed: 6232204]
62. Wood KJ & Goto R Mechanisms of Rejection: Current Perspectives: Transplantation 93, 1–10 (2012). [PubMed: 22138818]
63. Staquicini FI et al. Vascular ligand-receptor mapping by direct combinatorial selection in cancer patients. Proc. Natl. Acad. Sci. U. S. A 108, 18637–18642 (2011). [PubMed: 22049339]
64. Hua S Targeting sites of inflammation: intercellular adhesion molecule-1 as a target for novel inflammatory therapies. Front. Pharmacol 4, (2013).
65. Kwon EJ, Dudani JS & Bhatia SN Ultrasensitive tumour-penetrating nanosensors of protease activity. Nat. Biomed. Eng 1, 0054 (2017). [PubMed: 28970963]
66. Han D et al. Assessment of Cytotoxic Lymphocyte Gene Expression in the Peripheral Blood of Human Islet Allograft Recipients: Elevation Precedes Clinical Evidence of Rejection. Diabetes 53, 2281–2290 (2004). [PubMed: 15331537]
67. Jaffer FA & Weissleder R Molecular imaging in the clinical arena. JAMA 293, 855–862 (2005). [PubMed: 15713776]
68. Weissleder R, Tung C-H, Mahmood U & Bogdanov J In vivo imaging of tumors with protease-activated near-infrared fluorescent probes. Nat. Biotechnol 17, 375–378 (1999). [PubMed: 10207887]
69. Olson ES et al. Activatable cell penetrating peptides linked to nanoparticles as dual probes for in vivo fluorescence and MR imaging of proteases. Proc. Natl. Acad. Sci 107, 4311–4316 (2010). [PubMed: 20160077]
70. Sugahara KN et al. Tissue-penetrating delivery of compounds and nanoparticles into tumors. Cancer Cell 16, 510–520 (2009). [PubMed: 19962669]
71. Hori SS & Gambhir SS Mathematical Model Identifies Blood Biomarker–Based Early Cancer Detection Strategies and Limitations. Sci. Transl. Med 3, 109ra116–109ra116 (2011).
72. Lutz AM, Willmann JK, Cochran FV, Ray P & Gambhir SS Cancer Screening: A Mathematical Model Relating Secreted Blood Biomarker Levels to Tumor Sizes. PLOS Med. 5, e170 (2008). [PubMed: 18715113]
73. Dharnidharka VR, Kwon C & Stevens G Serum cystatin C is superior to serum creatinine as a marker of kidney function: A meta-analysis. Am. J. Kidney Dis 40, 221–226 (2002). [PubMed: 12148093]
74. Kaplan B, Schold J & Meier-Kriesche H-U Poor predictive value of serum creatinine for renal allograft loss. Am. J. Transplant. Off. J. Am. Soc. Transplant. Am. Soc. Transpl. Surg 3, 1560–1565 (2003).
75. Slocum JL, Heung M & Pennathur S Marking Renal Injury: Can We Move Beyond Serum Creatinine? Transl. Res 159, 277–289 (2012). [PubMed: 22424431]
76. Haase M et al. Accuracy of Neutrophil Gelatinase-Associated Lipocalin (NGAL) in Diagnosis and Prognosis in Acute Kidney Injury: A Systematic Review and Meta-analysis. Am. J. Kidney Dis 54, 1012–1024 (2009). [PubMed: 19850388]
77. Mischak H et al. Recommendations for Biomarker Identification and Qualification in Clinical Proteomics. Sci. Transl. Med 2, 46ps42–46ps42 (2010).
78. Prendergast MB & Gaston RS Optimizing Medication Adherence: An Ongoing Opportunity To Improve Outcomes After Kidney Transplantation. Clin. J. Am. Soc. Nephrol. CJASN 5, 1305–1311 (2010). [PubMed: 20448067]
79. Alangaden GJ et al. Infectious complications after kidney transplantation: Current epidemiology and associated risk factors. Clin. Transplant 20, 401–409 (2006). [PubMed: 16842513]

80. Sellarés J et al. Understanding the Causes of Kidney Transplant Failure: The Dominant Role of Antibody-Mediated Rejection and Nonadherence. Am. J. Transplant 12, 388–399 (2012). [PubMed: 22081892]

81. Palmacci S Synthesis of Polysaccharide Covered Superparamagnetic Oxide Colloids.

82. Presolski Stanislav I, Phong Hong Vu & Finn MG Copper-Catalyzed Azide–Alkyne Click Chemistry for Bioconjugation. Curr. Protoc. Chem. Biol 3, 153–162 (2011). [PubMed: 22844652]

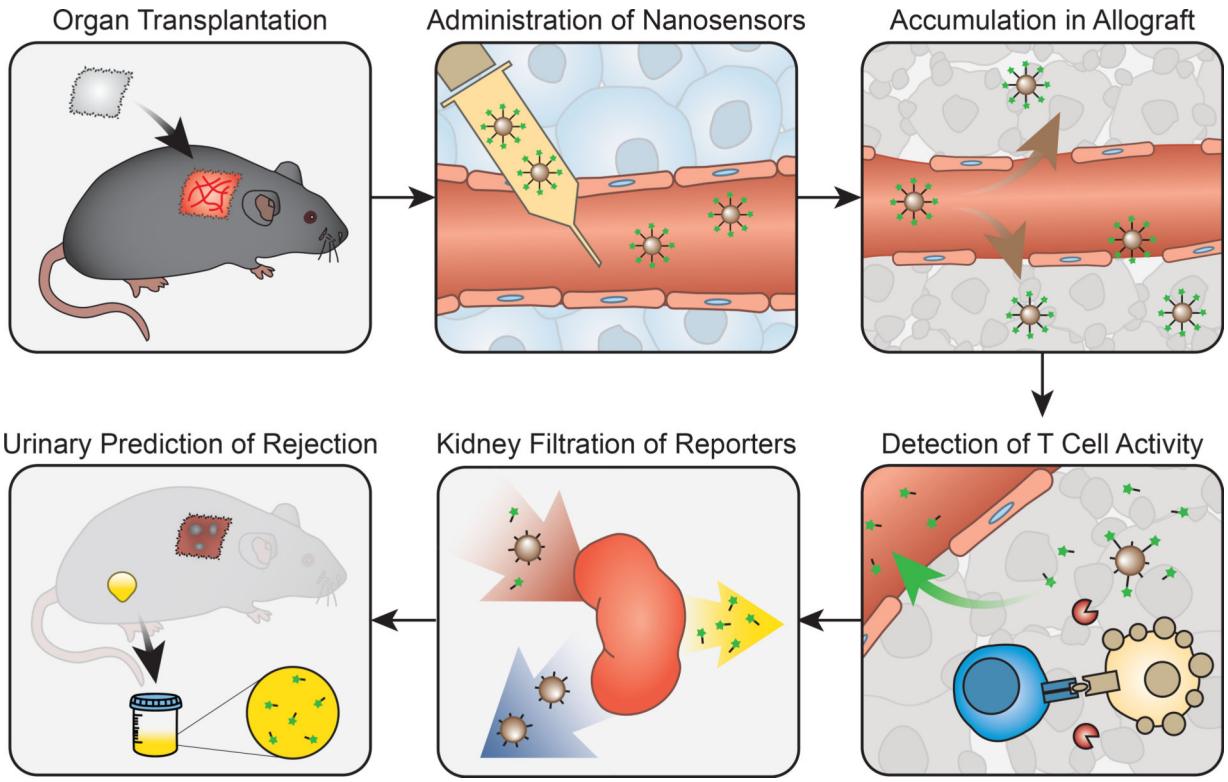

Fig. 1. Granzyme B activity nanosensors detect onset of acute allograft rejection by amplifying detection signals into urine.

In transplant recipients, GzmB activity nanosensors are intravenously administered and accumulate in allograft tissues. During onset of acute cellular rejection, GzmB secreted by alloreactive CD8 T cells cleaves peptide substrates on surface of nanosensors, triggering release of fluorescent reporters into urine. Urinary signals are quantified as early stage biomarkers of acute cellular rejection.

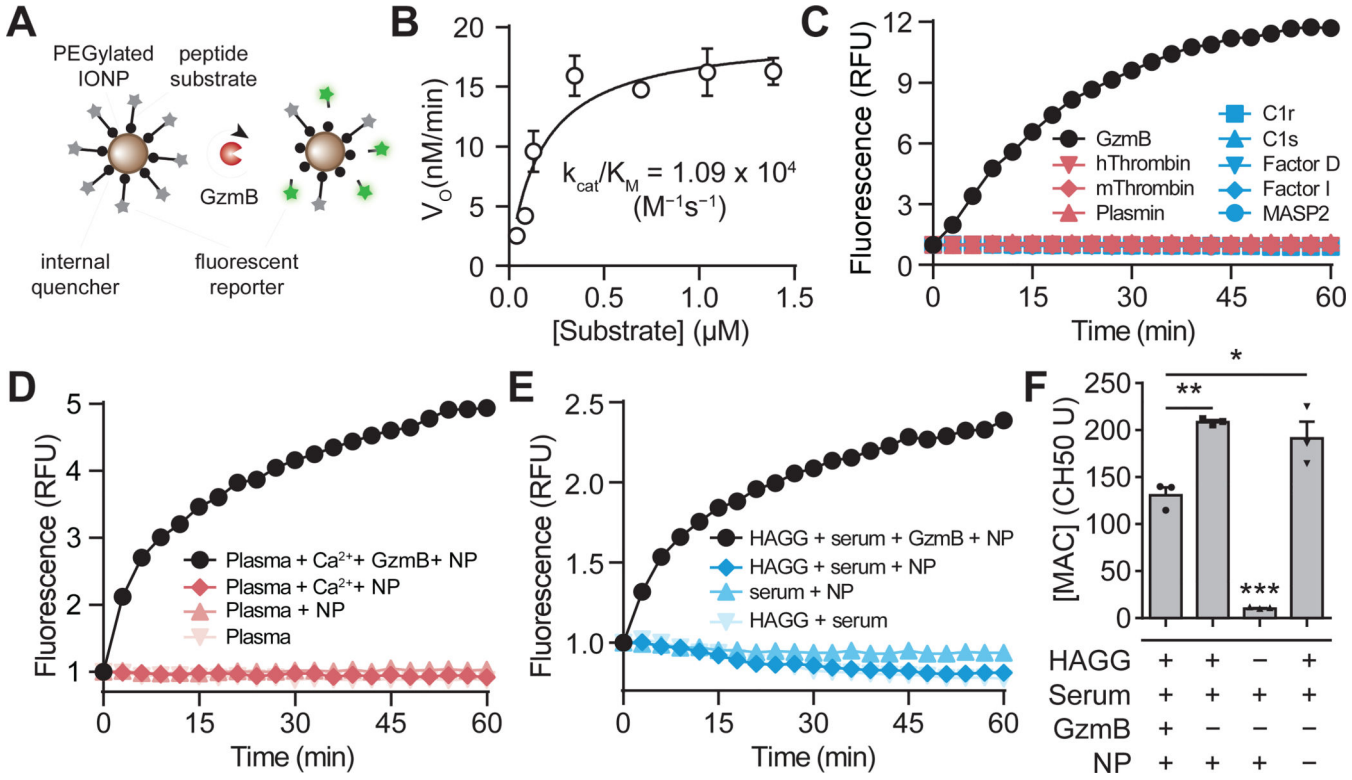

Fig. 2. Activity nanosensors detect proteolytic cleavage by GzmB.

(**A**) GzmB activity nanosensors consist of PEGylated IONPs functionalized with GzmB substrates. In the presence of GzmB, peptide substrates are cleaved and separates the fluorescent and quencher, leading to an increase in sample fluorescence. (**B**) Michaelis-Menten analysis of GzmB cleavage of nanosensor (n = 5, R^2 = 0.79). Data was fitted to GraphPad kcat equation (total enzyme concentration Et = 0.17 μM). (**C**) *In vitro* protease activity assays showing normalized fluorescence of activity nanosensor samples after incubation with GzmB (black) or proteases from coagulation (red) or complement (blue) cascades. This experiment was repeated independently 3 times with similar results. (**D**) Activity assays showing normalized fluorescence of mouse plasma samples spiked with nanoparticles (NP), GzmB, or Ca^{2+} to initiate coagulation. This experiment was repeated independently 3 times with similar results. (**E**) Activity assays showing normalized fluorescence of serum samples spiked with NPs, GzmB, or heat aggregated gamma globulin (HAGG) to initiate complement cascade. This experiment was repeated independently 3 times with similar results. (**F**) ELISA quantification of membrane attack complex (MAC) in activity assay supernatants of activity nanosensors with control serum and HAGG for complement activation (one-way ANOVA with Turkey's post-test and correction for multiple comparisons, *P< 0.05, **P < 0.01, n = 3). Concentration of MACs in test condition is proportional to CH50 U, which is defined as the volume dilution of serum that sufficiently lyses 50% of red blood cells in hemolytic reaction. Central values = means, and error bars = s.e.m.

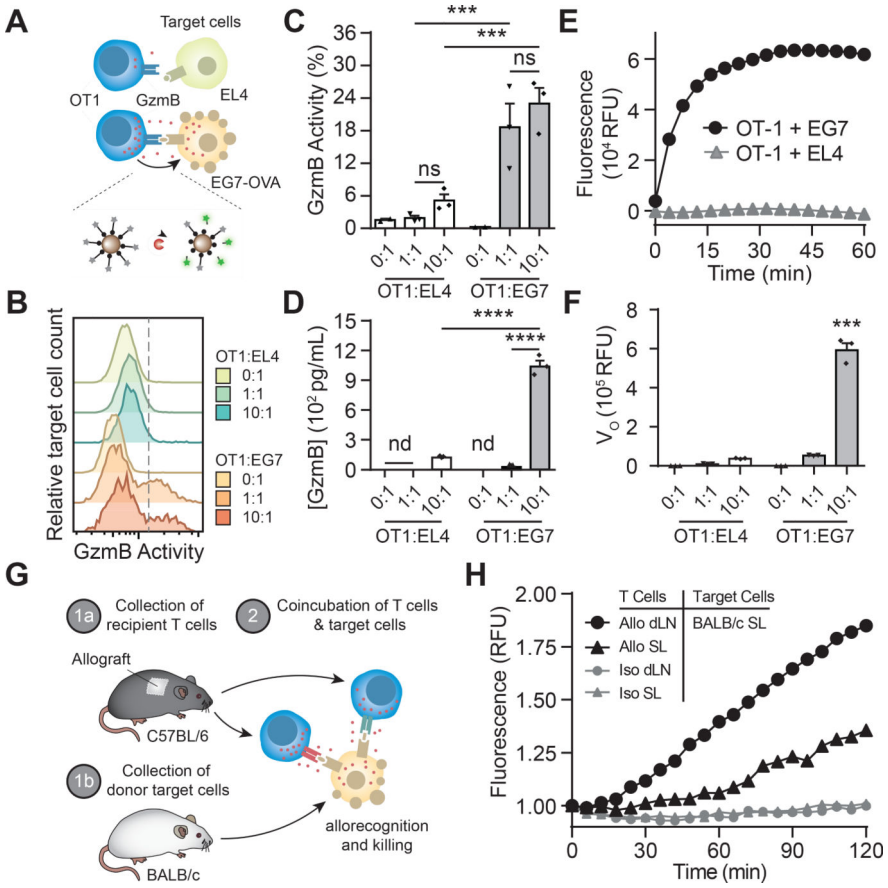

Fig. 3. Sensing GzmB activity during alloreactive T cell killing.

(**A**) After upregulating expression, activated OT1 T cells secrete GzmB that enter and mediate apoptosis of EG7-OVA target cells. (**B**) Flow cytometry plots of GzmB activity within EG7-OVA and EL4 target cells after co-cultured with OT1 T cells at various T cell to target cell ratios. (**C**) Quantified plot of flow analysis showing percent of target EG7-OVA and EL4 cells with intracellular GzmB activity (one-way ANOVA with Turkey's post-test and correction for multiple comparisons, ***P < 0.001, n = 3). Central values = means, and error bars = s.e.m. (**D**) ELISA assay measuring levels of GzmB in co-culture supernatants of OT1 T cells with EG7-OVA or EL4 target cells at different T cell to target cell ratios (one-way ANOVA and Turkey's post-test and correction for multiple comparisons, ****P < 0.0001, n = 3; nd = not detected). Central values = means, and error bars = s.e.m. (**E**) T cell activity assays showing normalized fluorescence of activity nanosensors in co-culture supernatants of OT1 T cells with EG7-OVA or EL4 target cells. This experiment was repeated independently 5 times with similar results. (**F**) Quantified plot of T cell activity assays showing fitted value of initial cleavage velocities (one-way ANOVA and Turkey's post-test and correction for multiple comparisons, ***P < 0.001, n = 3). Central values = means, and error bars = s.e.m. (**G**) Activity nanosensors sense GzmB secreted during alloreactive T cell killing. (**H**) T cell activity assays showing normalized fluorescence of activity nanosensors in co-culture supernatants of T cells isolated from spleen (SL) or draining lymph nodes (dLN) of skin graft mice with target cells from BALB/c donor mice. This experiment was repeated independently 3 times with similar results.

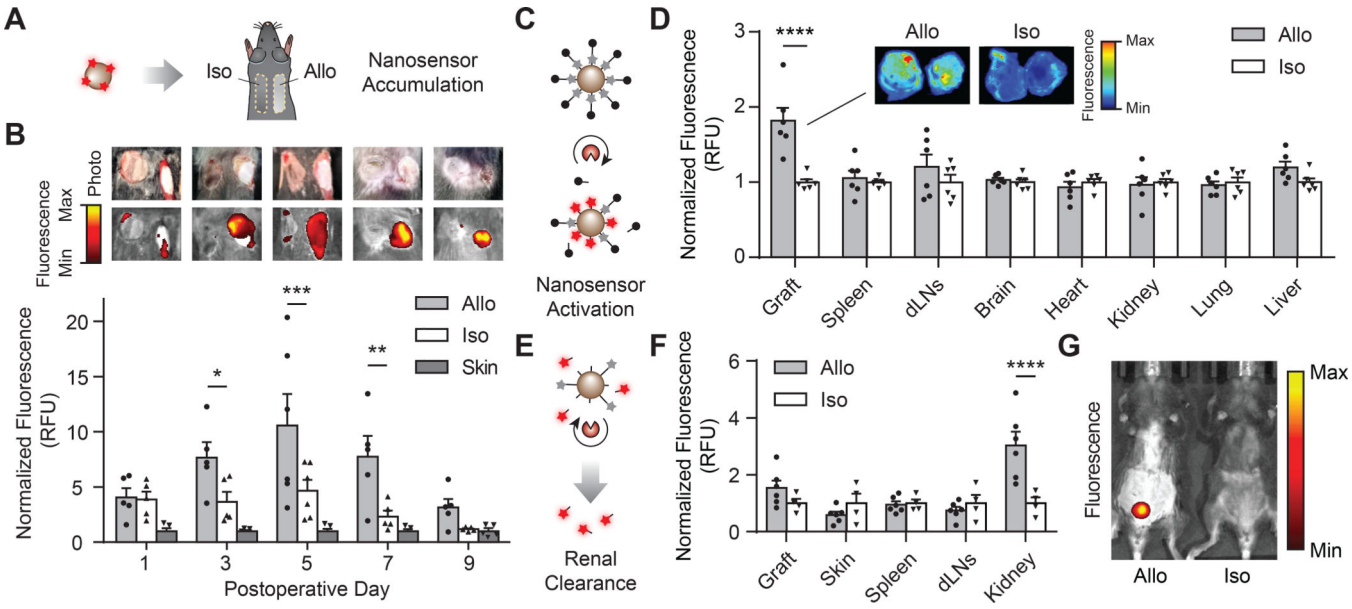

Fig. 4. Granzyme B activity during ACR triggers a urine pharmacokinetic switch.

(**A**) Mice bearing both isograft (Iso) and allograft (Allo) tissues are dosed with surface-labelled nanosensors for allograft accumulation and biodistribution studies. (**B**) *Top*, photographs of mice bearing dual skin grafts and corresponding near infrared (NIR) fluorescent images. *Bottom,* quantified fluorescent intensities of excised skin grafts (two-way ANOVA and Sidak post-test and correction for multiple comparisons, *P< 0.05, **P < 0.01, ***P < 0.001, n = 5 for PODs 1, 3, 7, 9 and n = 6 for POD 5). Fluorescent signals from different days were normalized by signals from healthy skin. Central values = means, and error bars = s.e.m. (**C**) Schematic of an NIR activatable probe that is conjugated with GzmB substrates containing internal fluorophores and terminal quenchers. After cleavage, the quencher is liberated to allow the nanoparticle to fluoresce. (**D**) Fluorescence of major organs harvested from allograft and isograft mice dosed with the NIR activatable probe. (two-way ANOVA and Sidak post-test and correction for multiple comparisons, ****P < 0.0001, n = 6). Fluorescent signals were normalized by signals from isograft mice. *Inset*, NIR fluorescent image of representative excised skin grafts. Central values = means, and error bars = s.e.m. (**E**) Mice bearing either skin allo- or iso-graft are dosed with activity nanosensors with terminal fluorophores, which can trigger a urine pharmacokinetic switch upon activation by GzmB during alloreactive T cell killing. (**F**) Fluorescence of tissue homogenates from allograft and isograft mice after administration of activity nanosensors (two-way ANOVA and Sidak post-test and correction for multiple comparisons, *P< 0.05, n = 4 isograft mice and n = 6 allograft mice). Fluorescent signals were normalized by signals from isograft mice. Central values = means, and error bars = s.e.m. (**G**) Whole body NIR fluorescent image after administration of activity nanosensors showing fluorescent signals from the bladders of allograft-bearing mice. This experiment was repeated independently 3 times with similar results.

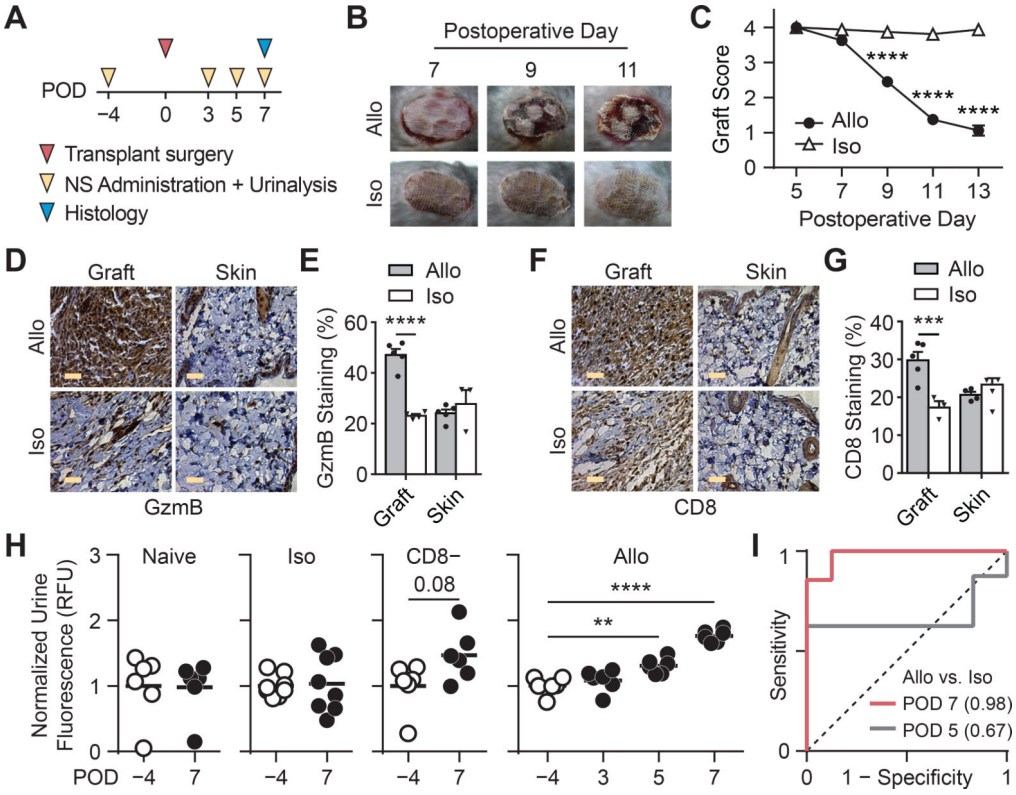

Fig. 5. Urinary prediction of ACR upon administration of GzmB activity nanosensors.

(**A**) Timeline of experimental procedures. POD = Postoperative Day. (**B**) Pictures of skin grafts showing morphological features of allograft rejection that begins to appear on POD 9. This experiment was repeated independently 5 times with similar results. (**C**) Skin graft scores showing graft quality between allo- and iso-grafts (two-way ANOVA and Sidak's post-test and correction for multiple comparisons, ****P < 0.0001, n = 8). (**D**) Immunohistochemistry staining of GzmB in graft and healthy skin tissues from mice bearing allo- or iso-grafts. Scale bars = 5 μm. This experiment was repeated independently 3 times with similar results. (**E**) Quantified plot of IHC data showing percent of GzmB staining in graft and skin tissues (two-way ANOVA and Sidak's post-test and correction for multiple comparisons, ****P < 0.0001, n = 4 fields of view for isograft mice and n = 5 for allograft mice). Central values = means, and error bars = s.e.m. (**F**) Immunohistochemistry staining of CD8 in graft and healthy skin tissues from mice bearing allo- or iso-grafts. Scale bars = 5 μm. This experiment was repeated independently 3 times with similar results. (**G**) Quantified plot of IHC data showing percent of CD8 staining in graft and skin tissues (two-way ANOVA and Sidak's post-test and correction for multiple comparisons, ***P < 0.001, n = 4 fields of view for isograft mice and n = 5 for allograft mice). Central values = means, and error bars = s.e.m. (**H**) *Left*, Normalized urine fluorescence after administration of activity nanosensors to naïve mice (n = 6), isograft mice (n = 8), and CD8 depleted allograft mice (paired two-sided Student's t-test, n = 6, P = 0.08; not significant). *Right*, normalized urine fluorescence after administration of nanosensors to allograft mice before and at selected days after transplant surgery (one-way ANOVA with Dunnett post-test and correction for multiple comparisons, **P < 0.01, ****P < 0.0001, n = 6). Urine signals were quantified as

percent injected dose before normalized by pre-transplant signals. (**I**) Receiver-operating-characteristic (ROC) analysis showing the diagnostic specificity and sensitivity of activity nanosensors in differentiating between allografts (n = 6) from isografts (n = 8) on POD 7 (AUC = 0.982, 95% CI = 0.937 – 1.027) and POD 5 (AUC = 0.667, 95% CI = 0.354 – 0.979).

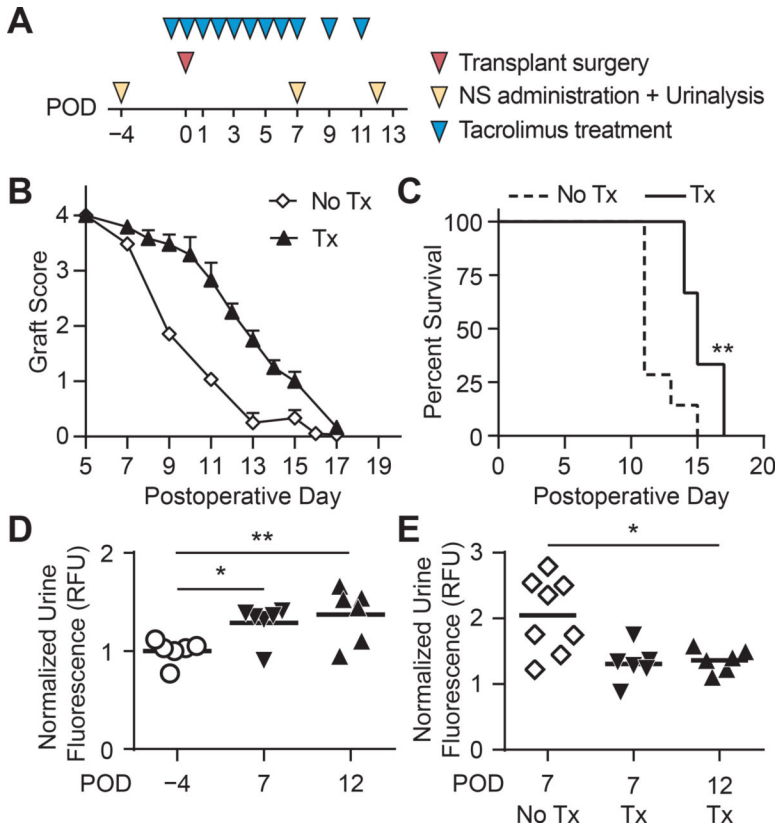

Fig. 6. Urinary prediction of allograft rejection under subtherapeutic immunosuppression

(**A**) Timeline of experimental procedures. (**B**) Skin graft scores quantifying allograft quality in mice given subtherapeutic doses of tacrolimus (n = 6) and untreated mice (n = 8). Central values = means, and error bars = s.e.m. (**C**) Kaplan-Meier survival analysis comparing cohorts of treated (n = 6) and untreated mice (n = 8) (Mantel-Cox test, **P < 0.01). (**D**) Quantified urine fluorescence after administration of nanosensors to tacrolimus-treated allograft bearing mice before (POD −4) and after transplantation (POD 7, 12) (one-way ANOVA with Dunnett post-test and correction for multiple comparisons, *P< 0.05, **P < 0.01, n = 6). Urine signals were quantified as percent injected dose before normalized by pre-transplant signals. (**E**) Fold increase in urine signals relative to pre-transplant signals in tacrolimus treated (PODs 7, 12, n = 6) and untreated (POD 7, n = 8) allograft mice (unpaired two-sided Student's t-test, *P< 0.05).